Integration of high-speed GaAs metal-semiconductor-metal photodetectors by means of transfer printing for 850 nm wavelength photonic interposers

GUANYU CHEN,[1,2,4] JEROEN GOYVAERTS,[2,4] SULAKSHNA KUMARI,[2] JORIS VAN KERREBROUCK,[3] MUHAMMAD MUNEEB,[2] SARAH UVIN,[2] YU YU[1,5] AND GUNTHER ROELKENS[2,*]

[1]*Wuhan National Laboratory for Optoelectronics & School of Optical and Electronic Information, Huazhong University of Science and Technology, Wuhan 430074, China*
[2]*Photonics Research Group, Ghent University - imec, Technologiepark 15, 9052 Gent, Belgium*
[3]*IDLab, Ghent University – imec, Technologiepark 15, 9052 Gent-Zwijnaarde, Belgium*
[4]*Contributed equally*
[5]*yuyu@mail.hust.edu.cn*
[*]*Gunther.Roelkens@UGent.be*

Abstract: We propose and demonstrate the integration of 850 nm GaAs-based metal-semiconductor-metal (MSM) photodetectors (PDs) based on transfer printing for application in photonic interposers. Both devices that directly interface with a multimode optical fiber (with device dimensions of 70 μm × 70 μm) as well as devices that interface with a SiN waveguide layer through a grating coupler (with device dimensions of 30 μm × 30 μm) are demonstrated. The dark currents are measured to be 22 nA and 7.2 nA at 2 V bias for the larger and smaller PDs respectively. For 850 nm wavelength, the external responsivities are measured to be 0.117 A/W and 0.1 A/W at 2 V bias. 20 GHz bandwidth is measured. Open 40 Gb/s eye diagrams are realized.

OCIS codes: (040.5160) Photodetectors; (130.0250) Optoelectronics; (200.4650) Optical interconnects; (250.5300) Photonic integrated circuits.

References and links

1. Alduino and M. Paniccia, "Interconnects: Wiring electronics with light," Nat. Photonics **1**(3), 153–155 (2007).
2. C. Sun, M. T. Wade, Y. Lee, J. S. Orcutt, L. Alloatti, M. S. Georgas, A. S. Waterman, J. M. Shainline, R. R. Avizienis, S. Lin, B. R. Moss, R. Kumar, F. Pavanello, A. H. Atabaki, H. M. Cook, A. J. Ou, J. C. Leu, Y. Chen, K. Asanovic, R. J. Ram, M. A. Popović and V. M. Stojanović, "Single-chip microprocessor that communicates directly using light," Nature **528**, 534–538 (2015).
3. A Narasimha, S. Abdaila, C. Bradbury, A. Clark, J. Clymore, J. Coyne, A. Dahl, S. Gloeckner, A. Gruenberg, D. Guckenberger, S. Gutierrez, M. Harrison, D. Kucharski, K. Leap, R. LeBlanc, V. Liang, M. Mack, D. Martinez, G. Masini, A. Mekis, R. Menigoz, C. Ogden, M. Peterson, T. Pinguet, J. Redman, J. Rodriguez, S. Sahni, M. Sharp, T. J. Sleboda, D. Song, V. Wang, B. Welch, J. Witzens, W. Xu, K. Vokoyama and P. D. DobbeIaere "An ultra low power CMOS photonics technology platform for H/S optoelectronic transceivers at less than $1 per Gbps," in Optical Fiber Communication Conference, OSA Technical Digest (online) (Optical Society of America, 2010), paper OMV4.
4. N. Ophir, K. Padmaraju, A. Biberman, L. Chen, K. Preston, M. Lipson, and K. Bergman, "First demonstration of error-free operation of a full silicon on-chip photonic link," in Optical Fiber Communication Conference, OSA Technical Digest (online) (Optical Society of America, 2011), paper OWZ3.
5. P. Dong, Y. K. Chen, T. Gu, L. L. Buhl, D. T. Neilson, and J. H. Sinsky, "Reconfigurable 100Gb/s Silicon Photonic Network-on-Chip," J. Opt. Commun. Netw. **7**(1), A37–A43 (2015).
6. Y. Urino, T. Usuki, J. Fujikata, M. Ishizaka, K. Yamada, T. Horikawa, T. Nakamura, and Y. Arakawa, "High-density and wide-bandwidth optical interconnects with silicon optical interposers," Photonics Res. **2**(3), A1–A7 (2014).
7. A. hayakawa, M. Kibune, A. Toda, S. Tanaka, T. Simoyama, Y. Chen, T. Akiyama, S. Okumura, T. Baba, T. Akahoshi, S. Ueno, M. Kazunori, M. Imai, J. H. Jiang, P. Thachile, T. Riad, S. Sekiguchi, S. Akiyama, Y. Tanaka, K. Morito, D. Mizutani, T. Mori, T. Yamamoto, and H. Ebe, "A 25 Gbps silicon photonic transmitter

and receiver with a bridge structure for CPU interconnects," in Optical Fiber Communication Conference, OSA Technical Digest (online) (Optical Society of America, 2015) , paper Th1G.2.
8. G. Chen, Y. Yu, and X. Zhang, "Monolithically mode division multiplexing photonic integrated circuit for large capacity optical interconnection," Opt. Lett. **41**(15), 3543–3546 (2016).
9. D. Liang, G. Roelkens, R. Baets, and J. Bowers, "Hybrid integrated platforms for silicon photonics," Materials **3**(3), 1782–1802 (2010).
10. M. J. R. Heck, J. F. Bauters, M. L. Davenport, J. K. Doylend, S. Jain, G. Kurczveil, S. Srinivasan, Y. Tang, and J. E. Bowers, "Hybrid Silicon Photonic Integrated Circuit Technology," IEEE J. Quantum Electron. **19**(4), 6100117 (2013).
11. X. Xie, Q. Zhou, E. Norberg, M. Jacob-Mitos, Y. Chen, Z. Yang, A. Ramaswamy, G. Fish, J. C. Campbell, and A. Beling, "High-Power and High-Speed Heterogeneously Integrated Waveguide-Coupled Photodiodes on Silicon-on-Insulator," IEEE J. Lightwave Technol. **34**(1), 73–78 (2016).
12. C. Zhang, S. Zhang, J. D. Peters, and J. E. Bowers, "8× 8× 40 Gbps fully integrated silicon photonic network on chip," Optica **3**(7), 785–786 (2016).
13. S. Kumari, E. P. Haglund, J. Gustavsson, A. Larsson, G. Roelkens, R. Baets, "Vertical-cavity silicon-integrated laser with in-plane waveguide emission at 850 nm," Laser Photon. Rev. **12**(2), 1700206(2018).
14. G. Roelkens, J. Brouckaert, D. Taillaert, P. Dumon, W. Bogaerts, D. Van Thourhout, R. Baets, R. Nötzel, and M. Smit, "Integration of InP/InGaAsP photodetectors onto silicon-on-insulator waveguide circuits," Opt. Express **13**(25), 10102–10108 (2005).
15. E. Menard, K. J. Lee, D.-Y. Khang, R. G. Nuzzo, and J. A. Rogers, "A printable form of silicon for high performance thin film transistors on plastic substrates," Appl. Phys. Lett. **84**(26), 5398–5400 (2004).
16. A. De Groote, P. Cardile, A. Z. Subramanian, A. M. Fecioru, C. Bower, D. Delbeke, R. Baets, and G. Roelkens, "Transfer-printing-based integration of single-mode waveguide-coupled III-V-on-silicon broadband light emitters," Opt. Express **24**(13), 13754–13762 (2016).
17. B. Corbett, R. Loi, W. Zhou, D. Liu, and Z. Ma, "Transfer print techniques for heterogeneous integration of photonic components," Progress in Quantum Electronics **52**, 1-17 (2017).
18. G. Muliuk, N. Ye, J. Zhang, A. Abbasi, A. Trindade, C. Bower, D. Van Thourhout, and G. Roelkens, "Transfer Print Integration of 40Gbps Germanium Photodiodes onto Silicon Photonic ICs," in 43th European Conference on Optical Communication (ECOC 2017) (2017), paper Th.PDP.C.4.
19. B. S. Rho, S. Kang, H. S. Cho, H. H. Park, S. W. Ha, and B. H. Rhee, "PCB-compatible optical interconnection using 45°-ended connection rods and via-holed waveguides," IEEE J. Lightwave Technol. **22**(9), 2128–2134 (2004).
20. M. Currie, F. Quaranta, A. Cola, E. M. Gallo, and B. Nabet, "Low-temperature grown GaAs heterojunction metal-semiconductor-metal photodetectors improve speed and efficiency," Applied Physics Letters **99**, 203502 (2011).
21. J. Brouckaert, "Integration of photodetectors on silicon photonic integrated circuits (PICs) for spectroscopic applications," Ph.D. dissertation, Dept. Inform. Technol., Ghent Univ., Ghent, Belgium, Oct. 2010.
22. J. B. D. Soole and H. Schumacher, "InGaAs metal-semiconductor-metal photodetectors for long wavelength optical communications," IEEE J. Quantum Electron. **27**(3), 737–752 (1991).
23. G. C. DeSalvo, A. Bozada Christopher, J. L. Ebel, D. C. Look, J. P. Barrette, C. L. A. Cerny, R. W. Dettmer, J. K. Gillespie, C. K. Havasy, T. J. Jenkins, K. Nakano, C. I. Pettiford, T. K. Quach, J. S. Sewell, and G. D. Via, "Wet chemical digital etching of GaAs at room temperature," J. Electrochem. Soc. **143**(11), 3652–3656 (1996).

1. Introduction

Optical interconnect is a potential candidate to solve the bandwidth bottleneck for both inter-chip and intra-chip communication [1, 2]. Although many networks-on-chip based on standard silicon photonics have been demonstrated, the lack of integrated laser sources makes the deployment of such interposers difficult, as dedicated packaging is required to interface with the external laser sources [2-8]. Hybrid integration of silicon photonics and III-V active components seems to be the best way to solve this problem [9-12]. While heterogeneous integration has mostly been geared towards operation in the 1310 nm or 1550 nm wavelength range, for photonic interposers 850 nm wavelength is a very attractive wavelength range due to the high-performance GaAs vertical cavity surface emitting laser (VCSEL) sources that are available and that operate at high ambient temperatures as can be expected on photonic interposers. Of course, operating at 850 nm wavelength requires modifying the silicon waveguide platform by using a SiN waveguide layer. The heterogeneous integration of 850nm GaAs VCSELs on such a waveguide platform was recently demonstrated [13]. Besides VCSELs, also photodetectors (PDs) need to be integrated. This can be realized using die-to-wafer bonding approaches [11, 12, 14]. However, when using die-to-wafer bonding to co-integrate the VCSELs and PDs, the millimeter-scale minimum die size prevents the

intermixed placement of laser sources and photodetectors as required for a photonic interposer. In this paper, we present the use of transfer printing [15-18] as a technique to overcome these issues.

The schematic of the photonic interposers based on the transfer printed PDs and VCSELs are shown in Fig. 1. The electronic integrated circuits (EICs) are flip-chipped onto the interposer. For communication between different modules, the data is transmitted through a multimode fiber (MMF) or a multi-mode waveguide in an underlying printed circuit board [19]. Communication on the same module (either for communication within one EIC or for communication between two EICs integrated on the same photonic interposer) is realized through SiN optical waveguides.

Among different kinds of PDs, metal-semiconductor-metal (MSM) PDs are advantageous because of their planar structure allowing for straightforward fabrication and low capacitance per unit area leading to high-speed performance. Therefore, in this paper transfer-printing-based, high-speed GaAs MSM PDs operating at 850 nm wavelength and suitable for both inter-module and intra-module interconnects are demonstrated. We elaborate on the design, fabrication, transfer printing and characterization of these devices. Two different photodetector sizes are discussed, a 30 μm × 30 μm device for intra-module interconnects and a 70 μm × 70 μm version for interfacing to multimode fiber for inter-module communication. Both the measured static and high-speed results of the two kinds of PDs validate that transfer printing holds great potential for the integration of such opto-electronic devices for future chip-scale interconnects.

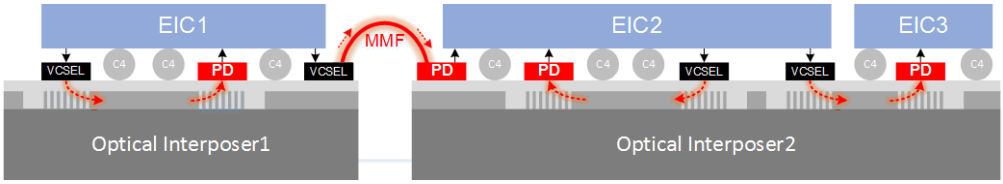

Fig. 1. The schematic structure of the chip-scale optical interconnection based on transfer printed PDs and VCSELs (EIC: electronic integrated circuit; C4: C4 solder balls; MMF: multimode fiber; black line: electrical path; red line: optical path).

2. Design

The MSM PD is based on two Schottky contacts, which are formed by directly depositing interdigitated metal electrodes onto the semiconductor material. The schematic structure of the MSM PD is shown in Fig. 2(a), which is composed of an absorption layer, a contact layer and the metal fingers. The thin contact layer with higher barrier height is used to lower the dark current and to facilitate charge transport to the contacts [20]. The two photodetector structures are shown in Figs. 2(b) and 2(c) respectively. Fig. 2(b) shows a normal incidence MSM PD interfacing with multimode fiber (MMF) with an active region of 70 μm × 70 μm, which is adapted to the diameter of a typical MMF. Fig. 2(c) shows the other MSM configuration, where it is printed on top of a silicon nitride (SiN) grating coupler (GC), which diffracts the light traveling inside the waveguide to the bottom surface of the MSM, where it is then absorbed. The size of this PD is adapted to the size of the grating coupler, and has an active region of 30 μm×30 μm as shown in Fig. 2(c). The larger PD was transfer printed onto a high-resistivity Si substrate for validating inter-chip interconnections, while the smaller one was transfer printed onto a SiN photonic integrated circuit for validating the intra-chip interconnection.

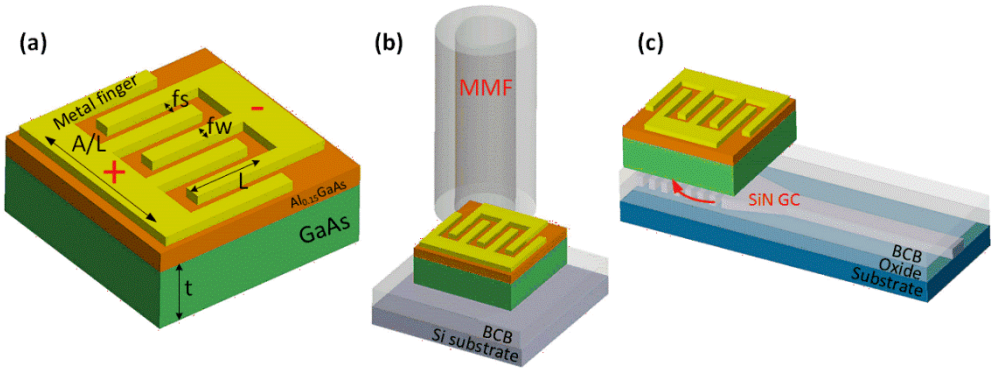

Fig. 2. (a) The schematic structure of the MSM PD. f_s : finger spacing; f_w : finger width; L: length; A: the total area of the active PD region; t: thickness. The MSM PDs (b) interfacing to multimode fiber and (c) a SiN waveguide.

Usually, RC parasitics and carrier transit time are the two main factors that limit the speed of a MSM PD [20]. Due to its thin planar structure, the parasitic capacitance is usually very low. The capacitance of the MSM PD is given by Eq. (1) [21].

$$C = \frac{K(k)}{K(k')}\varepsilon_0(1+\varepsilon_r)\frac{A}{f_s+f_w} = \frac{K(k)}{K(k')}\varepsilon_0(1+\varepsilon_r)(N-1)L \tag{1}$$

where ε_0 is the dielectric constant in free space, ε_r is the relative dielectric constant of the absorbing material, A is the total area of the active PD region, L is the active region length, N is the number of interdigitated fingers, f_s is the finger spacing and f_w is the finger width. $K(k)$ is the complete elliptic integral defined as Eq. (2).

$$K(k) = \int_0^{\pi/2} \frac{1}{\sqrt{(1-k^2\sin^2\varphi)}} d\varphi \tag{2}$$

with

$$k = \tan^2\left[\frac{\pi f_w}{4(f_s+f_w)}\right] \tag{3}$$

$$k' = \sqrt{1-k^2} \tag{4}$$

Based on these formulas, the calculated capacitance as a function of the finger spacing is shown in Fig. 3(a) for the two types of PDs, when the finger widths are 1.5, 2 and 2.5 μm. For the smaller MSM PD, the calculated capacitance is less than 30 fF. Even for the larger MSM PD, the capacitance is still less than 90 fF when the finger spacing is above 1.5 μm. Considering the carrier transit time to be determined by the finger spacing and the saturation carrier velocity [21, 22], the simulated bandwidth for these two types of PDs are shown in Fig. 3(b). When the finger spacing is wider than 1 μm, there is no big difference between these two types of PDs, because the carrier transit time is the main limiting factor. When the finger spacing is small enough, such as 0.2 μm, the MSM PD with the smaller active region will show its advantages due to its smaller RC parasitics. From the simulation results, it can be observed that the finger width has little influence on the speed of the device. For our experiments, nine different parameters combinations are used, as shown in Table 1, limited by the contact lithography process that was used to define the interdigitated electrodes.

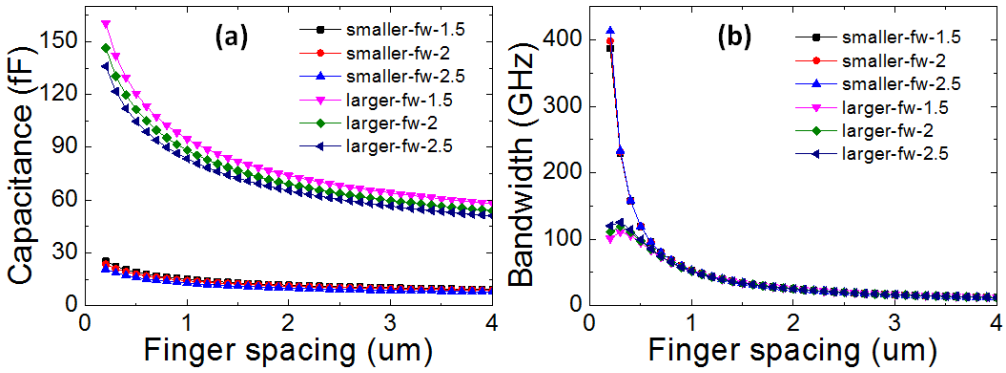

Fig. 3. The simulated (a) capacitance and (b) bandwidth as a function of finger spacing for three different finger widths for the smaller and larger MSM PDs.

Table 1. Combination of f_s and f_w values used in the experiments

No.	para-1	para-2	para-3	para-4	para-5	para-6	para-7	para-8	para-9
f_w (μm)	1.5	1.5	1.5	2	2	2	2.5	2.5	2.5
f_s (μm)	1.5	2	2.5	1.5	2	2.5	1.5	2	2.5

3. Device fabrication

The fabrication process of the transfer printed MSM PDs is shown in Fig. 4. We started from the epitaxial stack shown in Fig. 4(a) consisting of a 500 nm thick GaAs absorption layer and a 50 nm $Al_{0.15}GaAs$ contact layer. A GaAs (SAC 1) / AlAs (SAC 2) / GaAs (SAC 3) layer stack is used to protect the $Al_{0.15}GaAs$ contact layer. SAC 3 and SAC 2 layers are sequentially removed through wet etching using citric acid and HCl respectively. The last thin GaAs SAC 1 layer is removed through 3 cycles of digital etching, etching about 1.5 nm/cycle [23]. This method is chosen as it also removes the AlAs residues from the previous etch step [17] and results in a clean surface of the $Al_{0.15}GaAs$ contact layer. The cross section after removing the sacrificial layers is shown in Fig. 4(b). The interdigitated TiAu (4 nm and 85 nm thick respectively) metal fingers are then deposited onto the contact layer via lithography and lift-off, as shown in Fig. 4(c). It is important to note that there is a brief HCl-dip prior to the metal deposition to ensure that the native AlGaAs oxide is removed so that a good Schottky contact can be formed. Next, the absorption region mesa is defined, as shown in Fig. 4(d). Prior to the mesa etch, another $HCl:H_2O$ 1:1 dip is done to ensure the uniformity of the GaAs etch across the source substrate. The actual GaAs etch is done by a citric acid- H_2O_2 mixture. The release layer is patterned such that it will be accessible for the release etchant after the formation of the photoresist-based tethers in the next step (Fig. 4(e)). Here a number of digital etch steps are required in order to again remove any residues of the $Al_{0.9}GaAs$ release layer, which are difficult to avoid during the wet etch patterning. After the etching of the release layer, an additional citric acid-H_2O_2 etch is used to etch more deeply into the substrate for the photoresist tethers to adhere to. The photoresist tether structure was defined as described in [16]. A schematic top view image of the device structure after tether formation is shown in Fig. 4(f). The $Al_{0.9}GaAs$ layer is then released using an HCl 37% etch for 2 hours. Now the devices on the source wafer are ready to be transfer printed, as shown in Fig. 4(g).

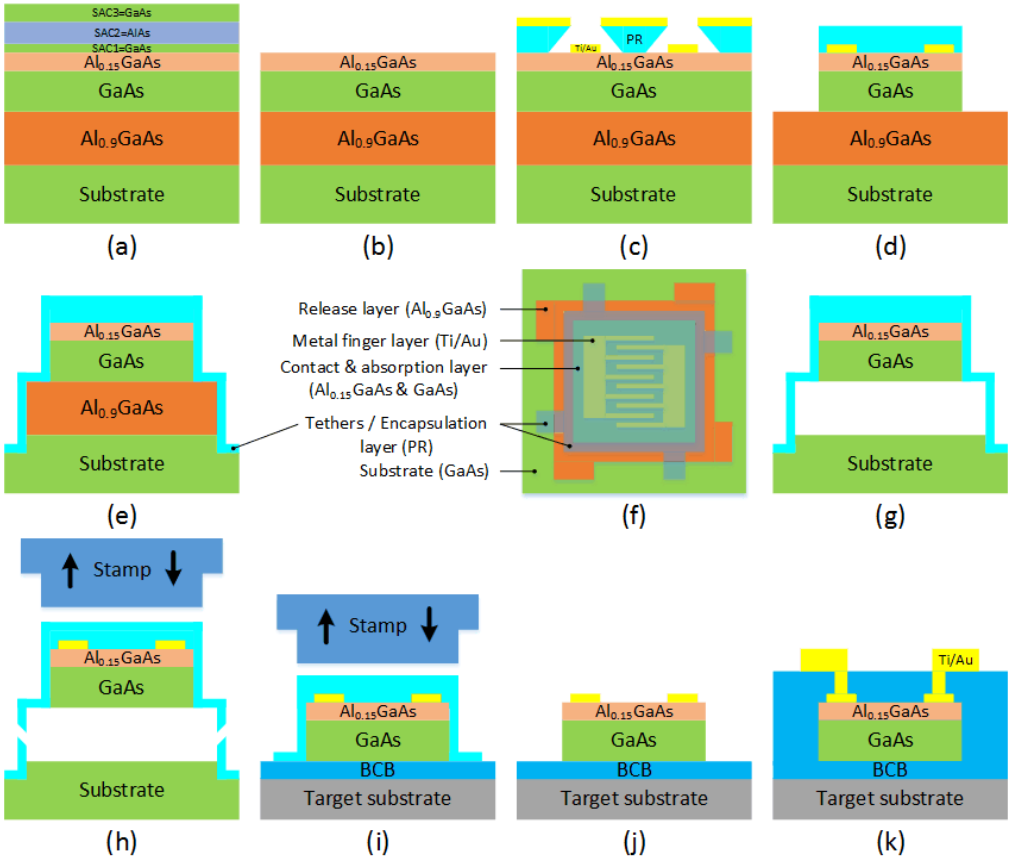

Fig. 4. Process flow for realizing and transfer printing MSM PDs. (a) GaAs epi stack; (b) removing the sacrificial layers; (c) metal fingers deposition; (d) patterning of mesa; (e) patterning of the release layer; (f) top view of the coupon after tether definition; (g) release etch of the devices; (h) device pick-up; (i) printing onto the target substrate; (j) removing the photoresist encapsulation; (k) patterning the DVS-BCB and deposition of the probe pads.

To evaluate the larger MSM PD coupons, a target Si wafer was prepared with thin, gold markers to align the devices during the printing process. 350 nm thick DVS-BCB (DVS-BCB-3022-35 1:1 mesithylene dilution) is spin coated onto this target substrate. Prior to printing, the target wafer is baked at 180℃ for 1.5 hour to partially cure the DVS-BCB adhesion layer. For the smaller MSM PD coupons, the target wafer with SiN waveguides and grating couplers were defined using e-beam lithography on a SiN-on-insulator substrate with 300 nm SiN waveguide layer thickness. The SiN GC has a uniform period of 718 nm, a filling factor (FF) of 52% and an etch depth of 300 nm. Similarly, 350 nm of DVS-BCB is spin coated onto the SiN target and cured at the same temperature (180℃) and for the same duration (1.5 hour). After these preparation steps, both target substrates are ready for transfer printing.

A X-Celeprint μTP-100 tool was used for transfer printing the devices from the source substrate to the target substrates. The MSM PDs are picked up at high velocity from the source substrate through a 20 μm×50 μm polydimethylsiloxane (PDMS) stamp, thereby breaking the tethers, as shown in Fig. 4(h). After that, the PD coupons are printed onto the prepared target substrate by laminating it and slowly lifting the stamp [18], as shown in Fig. 4 (i), leaving the MSM PDs attached to the target substrate. After transfer-printing, the photoresist encapsulation is removed using Reactive Ion Etching (RIE), as shown in Fig. 4(j).

After that, the target substrate is planarized using DVS-BCB (DVS-BCB-3022-35 undiluted). Vias are defined in the DVS-BCB to open the MSM pads on the coupon. In the final step, the metal pads are defined via lift-off, as shown in Fig. 4 (k). The microscope images of the final fabricated MSM PDs for both normal incidence and waveguide-coupling are shown in Fig. 5.

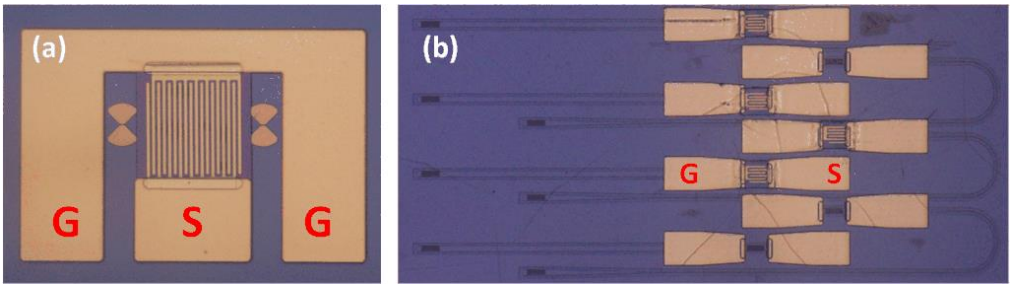

Fig. 5. Microscope images of the transfer printed (a) larger normal incidence PD with butterfly alignment markers in between the probe pads and (b) waveguide-coupled MSM PDs.

4. Characterization

The static behavior of the devices was first characterized. A source meter (Keithley 2400) is used to measure the dark current. The measured dark current for both larger and smaller coupons under different bias voltage are shown in Figs. 6 (a) and 6(b). The average dark currents for the different devices with nine parameters are 22 nA and 7.2 nA at 2 V bias for larger and smaller coupons respectively. For the photocurrent measurements, a fiber-coupled Ti:Sapphire laser operating at 850 nm was used. Before the input coupling fiber, a 50:50 splitter is used for monitoring the net input optical power. For the measurement of the waveguide-coupled PDs, a polarization controller (PC) before the coupling fiber is used to maximize the coupling efficiency to the waveguide, as the grating couplers used are optimized for TE polarized light. For the larger PDs, the responsivity is calculated using the optical power in the MMF, while for the waveguide-coupled detectors the optical power in the SiN waveguide is used. The measured responsivity for larger and smaller PDs are shown in Figs. 6(c) and 6(d). For the larger PDs, uniform and symmetrical IV curves are obtained for all nine different parameters. Smaller differences after the flat band voltage are attributed to the different filling factors of the metal finger configurations or may be due to slight measurement uncertainties/variations. The average external responsivity is 0.117 A/W at 2 V bias, which corresponds to a quantum efficiency of 17.2%. For the smaller PDs, larger deviations in responsivity are observed among the different parameters. The reason for the larger variation in these devices is currently not fully understood. The average responsivity is calculated to be 0.1 A/W under 2 V bias.

In principle, the high-speed performance of these two types PDs are the same, as the speed is limited by the transit time. Due to measurement limitations (lack of a high-speed single-mode-fiber-coupled directly modulated VCSEL at 850 nm), only the high-speed performance of the larger, normal incidence PDs are characterized, using a multimode-fiber-coupled high-speed VCSEL source. Firstly, the small signal measurement is performed using the setup shown in Fig. 7(a). The electrical signal from the vector network analyzer (VNA, Agilent N5247A) drives the vertical cavity surface emitting laser (VCSEL, VIS V50-850M) directly. The output modulated light from the VCSEL is vertically coupled to the MSM PD through the MMF. The converted electrical signal is then coupled back into the VNA. Meanwhile, the bias voltages of the VCSEL and MSM PD are applied using source meters via a bias-T. Before the measurement, the bandwidth of the VCSEL is first calibrated using a commercial high-speed PD (Optilab PD-40-MM-M). All the RF cables and high-speed GSG probe (Cascade) are also calibrated out. All devices with different parameters perform consistently. The measured S_{21} curves of one of these devices (para-1) is shown in Fig. 7(b).

There is a small roll-off at low frequency, which is attributed to an internal gain mechanism in the MSM, which can also be observed in the static characterization by the non-flat IV characteristic after the flat band voltage is reached. The bandwidth (neglecting the low frequency roll-off) is around 20 GHz for 2 V bias.

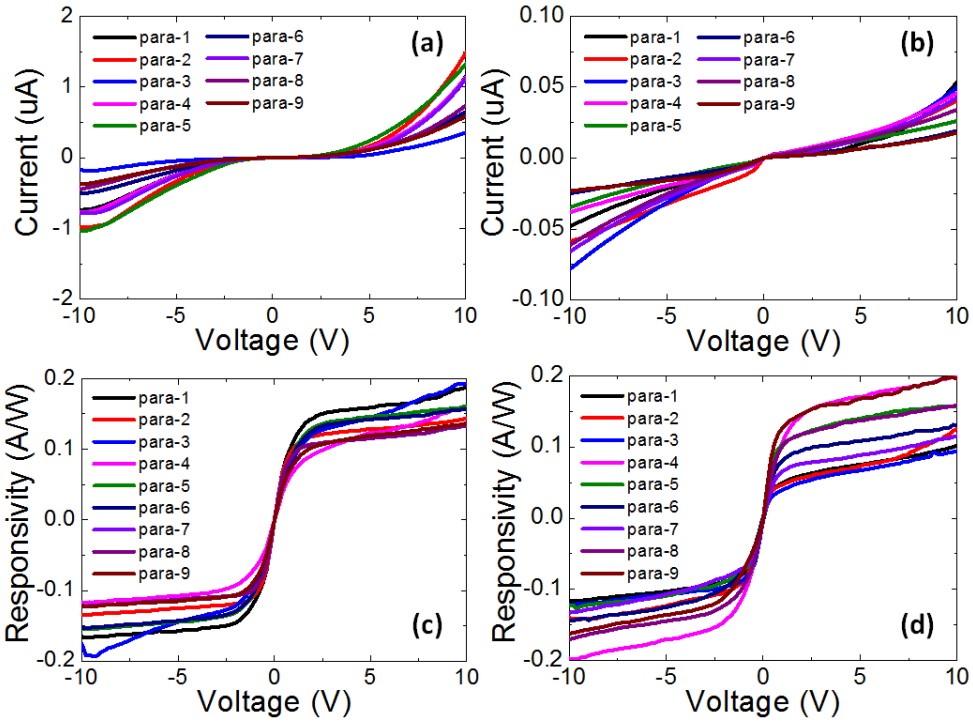

Fig. 6. The measured dark currents for (a) larger normal incidence and (b) small waveguide-coupled MSM PDs; the measured responsivity for (c) larger normal incidence and (d) small waveguide-coupled MSM PDs.

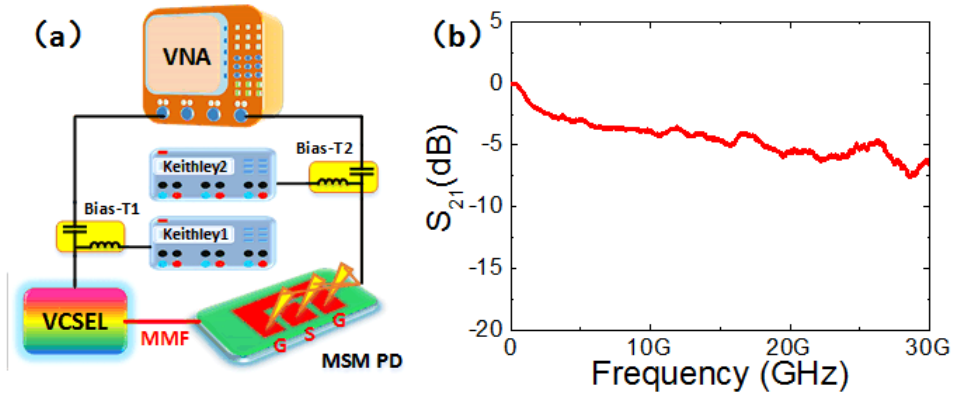

Fig. 7. (a) Small signal measurement setup. VCSEL: vertical cavity surface emitting laser; DUT: device under test; VNA: vector network analyzer. (b) The measured normalized S_{21} curve of the MSM PD (para-1) under 2 V bias.

The large signal measurements are then performed using the setup shown in Fig. 8(a). During the measurement, the multi-mode VCSEL is directly modulated by an arbitrary waveform generator (AWG, Agilent M9502A) with a pseudo random bit sequence (PRBS) of length $2^7 - 1$. The modulated light at 850 nm is vertically coupled to the MSM PD through

the MMF. The converted electrical signal from the PD is collected by a GSG probe and coupled to the digital signal analyzer (DSA, Keysight DSA-Z 634A), after being amplified (SHF S807). NRZ (10, 20, 30 and 40 Gb/s) signals are recorded under 2 V bias for the MSM PD (para-1) and are shown in Fig. 8 (b). Clear eye diagrams up to 40 Gb/s are observed. We did not observe significant differences among the different device parameters.

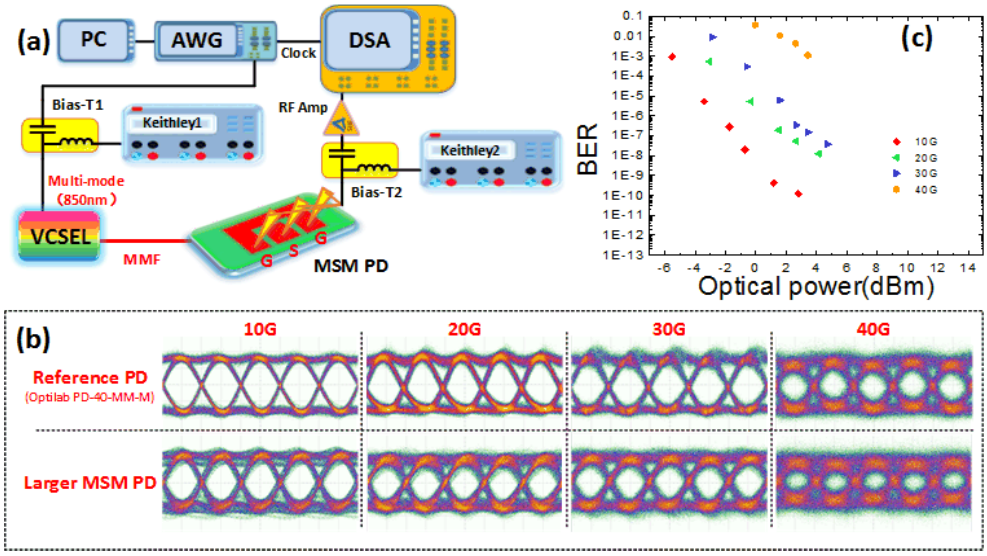

Fig. 8. (a) Setup of the large signal measurement. AWG: arbitrary waveform generator; PC: computer; RF amp: radio frequency amplifier; DSA: digital signal analyzer. (b) The measured (b) eye diagrams and (c) BER for different bit rates under 2V bias.

The BER measurements were performed based on the same measurement setup, using post-processing in MATLAB to analyze the complete recorded information from the DSA. The BER results for the 70 μm × 70 μm MSM PD (para-1) are shown in Fig. 8(c). It is worth to note that the MSM PD under test is not integrated with a trans-impedance amplifier (TIA), which has an important influence on the BER results and sensitivity. The bandwidth of the MSM PD is expected to be further improved by narrowing the metal finger spacing through more advanced lithography.

5. Conclusions

We propose and demonstrate high-speed 850 nm GaAs MSM photodetectors for photonic interposers integrated by means of transfer printing technology. Both surface illuminated devices, for module-to-module communication using MMF, and waveguide-coupled devices for intra-module communication via a SiN waveguide layer are demonstrated. Together with the development of 850 nm VCSELs integrated on the SiN waveguide platform, this will enable the realization of 850 nm photonic interposers for next-generation computing systems.

Funding

This work was funded by the ECSEL MicroPrince project and the BOF GOA project “Flexible Electronic Photonic Integration Platform” of Ghent University. This work is partially supported by the National Natural Science Foundation of China (Grant No. 61775073).

Acknowledgement

The authors would like to thank Steven Verstuyft and Liesbet Van Landschoot for the help with processing. Guanyu Chen would like to thank the Chinese Scholarship Council (CSC) for sponsoring his study at Ghent University.